Nano Research

Open Access

Research Article

Microfluidic-synthesized Sn^{4+}/Mg^{2+} co-doped zinc oxide for highly efficient and stable blue ZnSeTe QLEDs

Chunrui Da[1,2,§], Liming Xie[2,§] ✉, Weifeng Wang[2], Ting Wang[2], Yuan-Qiu-Qiang Yi[2], Jinyong Zhuang[3], Xiuqing Meng[3], Wenming Su[2] ✉, Tianzhi Yu[1] ✉, and Zheng Cui[2]

[1] *Key Laboratory of Opto-Electronic Technology and Intelligent Control (Ministry of Education), Lanzhou Jiaotong University, Lanzhou 730070, China*
[2] *Printable Electronics Research Center, Nano Devices and Materials Division, Suzhou Institute of Nano-Tech and Nano-Bionics, Chinese Academy of Sciences, Suzhou 215123, China*
[3] *Optoelectronics and Display Printing Technology (Nantong) Co., Ltd, 60 Chongzhou Avenue, Nantong 226000, China*
§ *Chunrui Da and Liming Xie contributed equally to this work.*

Cite this article: *Nano Research*, **2026**, *19*, 94908518. https://doi.org/10.26599/NR.2026.94908518

ABSTRACT: Mg-doped ZnO (ZMO) nanocrystal (NC) has been widely used as an electron transport layer (ETL) in quantum dot (QD) light-emitting diodes (QLEDs). However, its abundant oxygen vacancy (O_V) defects, high chemical activity and poor reproducibility of synthesis severely degrade device performance and shelf stability, limiting the practical application in display. To address these challenges, high-quality Sn^{4+}/Mg^{2+} co-doped ZnO (ZMSO) NCs were synthesized via a microfluidic (MF) reactor in the present study. This co-doping strategy effectively suppresses the O_V defects formation, increases the conduction band and electrical resistivity to enhance charge balance, as well as enhances the chemical stability of NCs to mitigate unstable chemical reaction during storage. Furthermore, the MF synthesis of NCs ensured consistent reproducibility and scalability. Based on the new ZMSO-based ETL, a remarkable enhancement of ZnSeTe blue QLED performance has been achieved, with a 2-fold increase in external quantum efficiency (EQE) from 9.6% to 19.7% and a 4.6-fold improvement in lifetime (@100 cd·m^{-2}) from 3931 to 18,236 h. Notably, the ZMSO-based device exhibited lower efficiency roll-off at high luminance and superior shelf stability compared to ZMO-based devices, offering an effective approach to achieving highly efficient and stable Cd-free blue QLEDs toward practical applications.

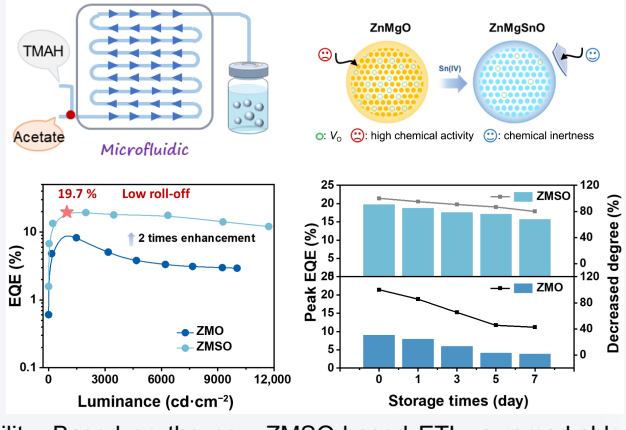

KEYWORDS: co-doped ZnO, microfluidic, electron transport layer, ZnSeTe, quantum dot light-emitting diodes (QLEDs)

1 Introduction

Quantum dot (QD) light-emitting diodes (QLEDs) have emerged as a promising technology for next-generation lighting and high-definition displays, owing to their wide color gamut, exceptional color saturation, and solution-processable fabrication [1–8]. Among various QD systems, cadmium (Cd)-based QDs have achieved rapid development, with operational lifetimes approaching to commercial standards [9–11]. However, the inherent chemical and environmental toxicity limit their applications in display [12–15]. For these reasons, nooxic and heavy metal-free QDs such as InP-based red/green QLEDs and ZnSeTe-based blue QLEDs have attracted growing attention [16–20]. Nevertheless, the performance characteristics of blue QLEDs still far lag behind red and green counterparts, including efficiency roll-off issue and low operational stability [21, 22]. Therefore, enhancing ZnSeTe-based blue QLEDs is critical for advancing eco-friendly QLED technology.

The electroluminescent performance of QLEDs is critically dependent on balanced carrier (electron and hole) injection and

Received: October 30, 2025; **Revised:** January 3, 2026
Accepted: February 1, 2026

✉Address correspondence to Liming Xie, lmxie2014@sinano.ac.cn; Wenming Su, wmsu2008@sinano.ac.cn; Tianzhi Yu, yutzh@mail.lzjtu.cn

effective radiative recombination within the QDs emitting layer. In ZnSeTe-based blue QLEDs, ZnMgO nanocrystal (ZMO NC) has been most frequently used as electron transport layer (ETL) [23–25]. By precisely controlling the magnesium (Mg) doping ratio in ZMO NC, the band structure and electron mobility of the ETL can be effectively modulated [20, 26, 27]. This modulation suppresses excessive electron injection and promotes balanced carrier distribution in the emission layer. However, ZMO also has interfacial electronic compatibility issues, including surface defects and lattice mismatch, which act as nonradiative centers to quench the exciton emission of QDs [28–31]. In addition, the high chemical activity of ZnMgO NC can cause poor shelf stability with uncontrollable performance in the QLEDs, which is unacceptable in practical applications [32–35].

To tackle the aforementioned negative effects, previous studies predominantly employed ligand encapsulation or water/acrylic acid treatments to passivate or isolate the surface defects [36–39]. For example, Shi et al. reported mercaptopropionic acid (MPA) capped ZMO (MPA-ZMO) NC to effectively suppresses the surface defects and regulate the energy band structure [39]. Jin et al. recently employed a straightforward water treatment of blue QLEDs to passivate the ZMO, achieving high current efficiency of 37.1 cd·A^{-1} and unprecedented stability with a remarkably long lifetime T_{95} of 287 h at 1000 cd·m^{-2} [40]. Despite the encouraging progresses, it should be noted that these "post-repair" strategies fail to eliminate the lattice defects formed during crystal growth, and is difficult to fundamentally eliminate the unstable nature of ZnMgO NC [40–43]. Moreover, the inherent inhomogeneity in conventional one-pot synthetic reactions causes significant variations in device performance and poor batch-to-batch stability, seriously hindering their practical application in display panel manufacturing [44–46].

In this study, a microfluidic (MF) synthesis strategy was proposed to realize high-valent metal doping to achieve high-quality Sn^{4+}/Mg^{2+} co-doped ZnO (ZMSO) NCs as ETLs (Fig. 1(a)). Compared to Zn^{2+}/Mg^{2+}, the higher oxidation state of Sn^{4+} with abundant metal–oxygen (M–O) bonds effectively reduced oxygen vacancy (O_V) defects in NCs, suppressing the formation of non-radiative recombination centers. Additionally, Sn^{4+}/Mg^{2+} co-doping not only upshifted the energy band, mitigating excess electron injection for the efficiency of hole–electron recombination in the emitting layer, but also enhanced the chemical stability of NCs to mitigate unstable chemical reaction under storage conditions (Fig. 1(b)). Furthermore, the MF synthesis platform enabled precise control over reaction kinetics and mixing, ensuring consistent production reproducibility and scalability. With the new ZMSO ETL, the overall performance of ZnSeTe-based blue QLEDs had

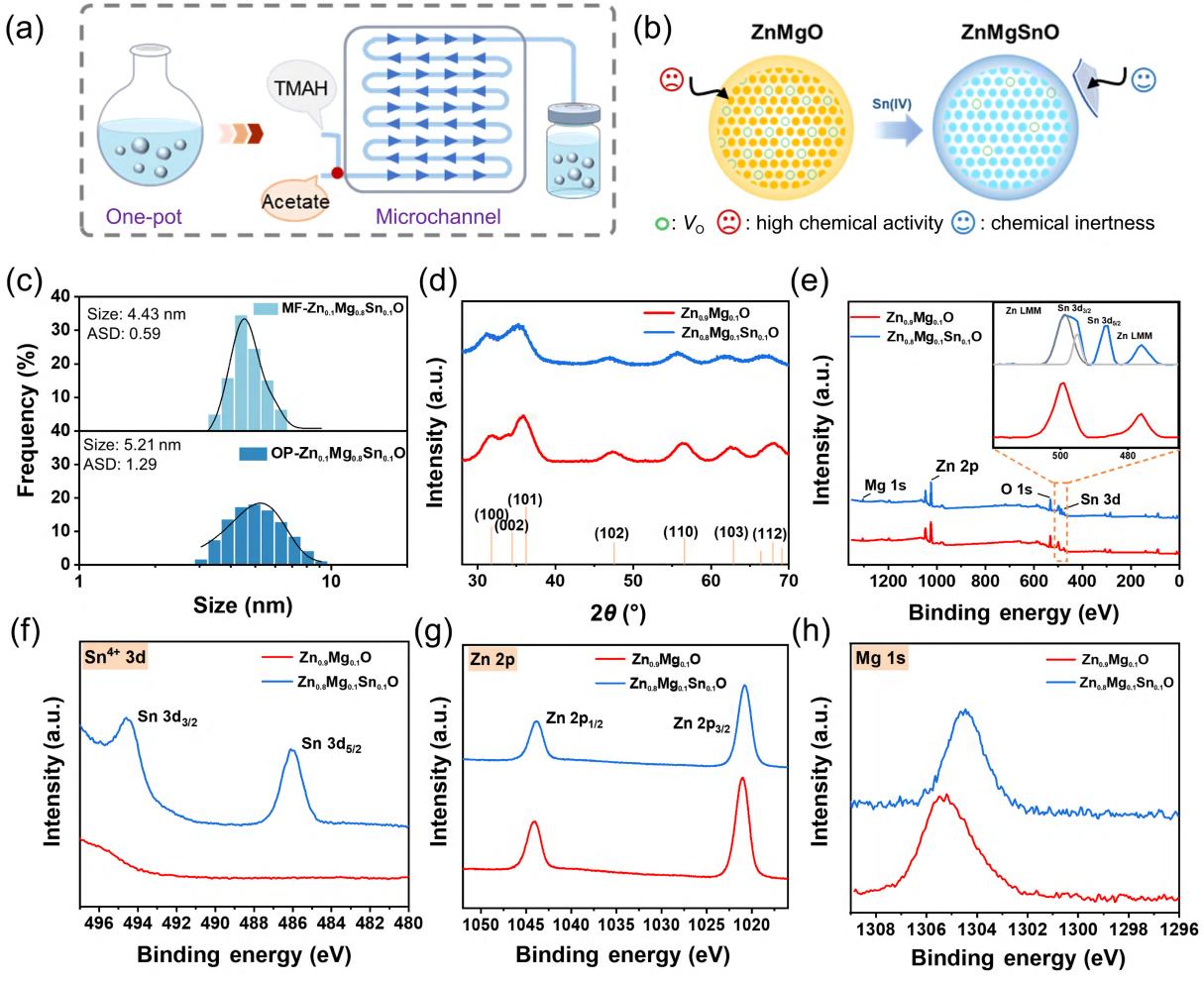

Figure 1 (a) Illustrations of the OP and the MF reactor. (b) Structural simulation of ZnMgO and ZnMgSnO NCs. (c) Size distribution of $Zn_{0.8}Mg_{0.1}Sn_{0.1}O$ NCs synthesized by MF and OP. (d) XRD spectra and (e) XPS spectra, comparison of high-resolution XPS scans of (f) Sn^{4+} 3d, (g) Zn 2p, and (h) Mg 1s photoelectron peaks of $Zn_{0.9}Mg_{0.1}O$ and $Zn_{0.8}Mg_{0.1}Sn_{0.1}O$ NCs.

been substantially boosted, showing a 2-fold increase in external quantum efficiency (EQE) from 9.6% to 19.7% and a 4.6-fold improvement in lifetime (@100 cd·m^{-2}) from 3931 to 18,236 h. In addition, the ZMSO-based device demonstrated lower efficiency roll-off at high luminance and extraordinary shelf stability compared to that based on ZMO. This new strategy paves the way to the development of highly efficient and stable Cd-free blue QLEDs for practical display applications.

2 Results and discussion

2.1 Characterization of ZMO and ZMSO NCs

Figure 1(a) is the schematic diagrams of the conventional one-pot (OP) and the new microfluidics (MF) synthesis routes. In the OP route, all reactants are introduced simultaneously into the reaction vessel. The initial reactant concentrations and reaction rates are relatively high, but as the reaction progresses, reactant consumption reduces the generation rate. This process can disrupt uniform nucleation and growth of NCs, leading to broad size distributions and poor batch-to-batch reproducibility. In contrast, the MF route employs miniature reaction containers where reactants are continuously supplied and rapidly mixed in the microchannel, enabling high-efficiency heat and mass transmission [47]. The result was that MF-synthesized $Zn_{0.8}Mg_{0.1}Sn_{0.1}O$ (average size: 4.43 nm, standard deviation: 0.59) and $Zn_{0.9}Mg_{0.1}O$ NCs (average size: 4.73 nm, standard deviation: 0.73) exhibited narrower size distributions than OP-based $Zn_{0.8}Mg_{0.1}Sn_{0.1}O$ (average size: 5.21 nm, standard deviation: 1.29) and $Zn_{0.9}Mg_{0.1}O$ NCs (average size: 5.52 nm, standard deviation: 1.3) (Fig. 1(c) and Fig. S1 in the Electronic Supplementary Material (ESM)). Meanwhile, we measured the particle size of MF- and OP-based $Zn_{0.8}Mg_{0.1}Sn_{0.1}O$ synthesized in different batches, as shown in Fig. S2 in the ESM. It can been seen that the size distributions fluctuation of MF-based NCs is smaller than that of OP, which is conducive to the better batch-to-batch stability of subsequent device performances.

Figures S3 and S4 in the ESM are the surface morphologies of NC films by atomic force microscopy (AFM). The root-mean-square (RMS) roughness values for MF-based films (1.187 nm for $Zn_{0.9}Mg_{0.1}O$, and 0.968 nm for $Zn_{0.8}Mg_{0.1}Sn_{0.1}O$) were lower than those of OP-based films (2.005 nm for $Zn_{0.9}Mg_{0.1}O$, and 1.885 nm for $Zn_{0.8}Mg_{0.1}Sn_{0.1}O$), attributing to their more uniform particle size distribution. The reduced roughness can promote better electrical contact between QDs and the electron transport layer, avoiding voids and irregularities at the interface and thus promoting more efficient carrier injection. Furthermore, we investigated the storage stability of ZMSO based on MF synthesis. It was found that the dispersion and particle size of ZMSO did not change significantly after three weeks as shown in Fig. S5 in the ESM, indicating good storage stability. Unless specified otherwise, all the subsequent characterizations are conducted on the NCs synthesized by the MF route.

To investigate the effect of Sn^{4+} and Mg^{2+} doping on the crystal structure of ZnO NCs, we performed X-ray diffraction (XRD) analysis on $Zn_{0.9}Mg_{0.1}O$, $Zn_{0.85}Mg_{0.1}Sn_{0.05}O$, $Zn_{0.8}Mg_{0.1}Sn_{0.1}O$, and $Zn_{0.75}Mg_{0.1}Sn_{0.15}O$ samples (Fig. 1(d) and Fig. S6 in the ESM). All NCs exhibited similar diffraction peaks in the (100), (002), (101), (102), (110), (103), and (112) directions, confirming the hexagonal wurtzite structure [48]. Furthermore, it can be observed that the (002) peak disappears and the diffraction peak blue-shifts and widens with the increase of Sn doping ratio, attributing to the increase in lattice strain and reduced crystallinity [48–50]. However, no other parasitic peaks were found in the XRD pattern, indicating the absence of phase segregation. As reported, the ionic radius of Mg^{2+} (71 pm) and Sn^{4+} (69 pm) are similar to that of Zn^{2+} (74 pm), allowing efficient incorporation of these dopants into the ZnO lattice without significant structural distortion [51].

Subsequently, we further employed X-ray photoelectron spectroscopy (XPS) to verify Sn^{4+} and Mg^{2+} doping. As shown in Fig. 1(e), no Sn signal was detected in the pristine $Zn_{0.9}Mg_{0.1}O$ NCs from the whole detecting range, whereas $Zn_{0.8}Mg_{0.1}Sn_{0.1}O$ NCs exhibited clear Sn 3d signals, confirming successful Sn doping. In detail, the Sn 3d signal could be carefully deconvoluted into several features (Fig. 1(f)). The features at binding energies of ~ 494 and 486 eV for Sn $3d_{3/2}$ and Sn $3d_{5/2}$ signals are in agreement with the binding energy of Sn^{4+} as in SnO_2, which indicates the existence of Sn^{4+} valence states in ZMSO NCs. Additionally, compared to ZMO, the peaks related to Zn 2p and Mg 1s in the ZMSO show 0.2 eV and 0.75 eV shift to low binding energy, which is caused by the incorporation of Sn into the ZMO lattice (Figs. 1(g) and 1(h)) [52].

It is worth noting that the high-valent Sn^{4+} provides more abundant metal–oxygen bonds, which could effectively fill the oxygen vacancy (O_V) sites in ZMO. O_v and hydroxyl bonding (O_H) defects act as the trap states, readily capturing the excited electrons in QD, leading to severe interfacial exciton quenching and weak QD emission [34, 38, 42, 53]. To quantitatively compare the defects of ZMO and ZMSO films, we further analyzed the high-resolution O 1s XPS spectra, which were fitted with Gaussian–Lorentzian sub-peaks. As depicted in Figs. 2(a) and 2(b) and Fig. S7 in the ESM, the O 1s was deconvoluted into three peaks: metal-oxygen (O_M, ~ 530 eV), O_V (~ 531.3 eV), and O_H (~ 532.4 eV), respectively [47, 54]. The curve fitting provides full width at half maximum (FWHM) values and peak weightings (Table S1 in the ESM) of various components Notably, Sn doping into ZMO significantly decreases O_V concentration. Additionally, when the doping ratio of Sn is 10%, the O_V and O_H defect states are both reduced. The defect states in NCs could be observed through the photoluminescence (PL) spectroscopy as shown in Fig. 2(c). The excitation wavelength of PL spectra was 280 nm. In $Zn_{0.9}Mg_{0.1}O$ film, a strong and broad visible emission spectrum corresponding to defects luminescence was observed, while the visible emission intensities substantially decrease in $Zn_{0.8}Mg_{0.1}Sn_{0.1}O$. These results demonstrate that the Sn doping can passivate the electron trap states in the ETL, thereby effectively prevent the quenching of excitons at the QD/ETL interface.

2.2 The effect on ETL/QD interfaces

The steady-state temperature-dependent PL measurements of ZnSeTe QDs deposited on different substrates (quartz, quartz/$Zn_{0.9}Mg_{0.1}O$, quartz/$Zn_{0.8}Mg_{0.1}Sn_{0.1}O$) were performed to observe the effects of ETLs on the QD emission. As shown in Figs. 2(d)–2(f), the PL spectra of QDs on all different substrates exhibited a redshifted and decreased intensity as the temperature increased from 77 to 297 K, which is attributed to the temperature-dependent bandgap shrinkage in QDs [55, 56]. Figure S8 in the ESM presents the evolution of normalized integrated PL intensities with temperature variation. Notably, the PL intensity of QDs/$Zn_{0.9}Mg_{0.1}O$ decreased sharply with rising temperature, which arise from the interfacial exciton thermal quenching caused by massive defect states in the $Zn_{0.9}Mg_{0.1}O$ NCs. In contrast, the PL intensities of QDs

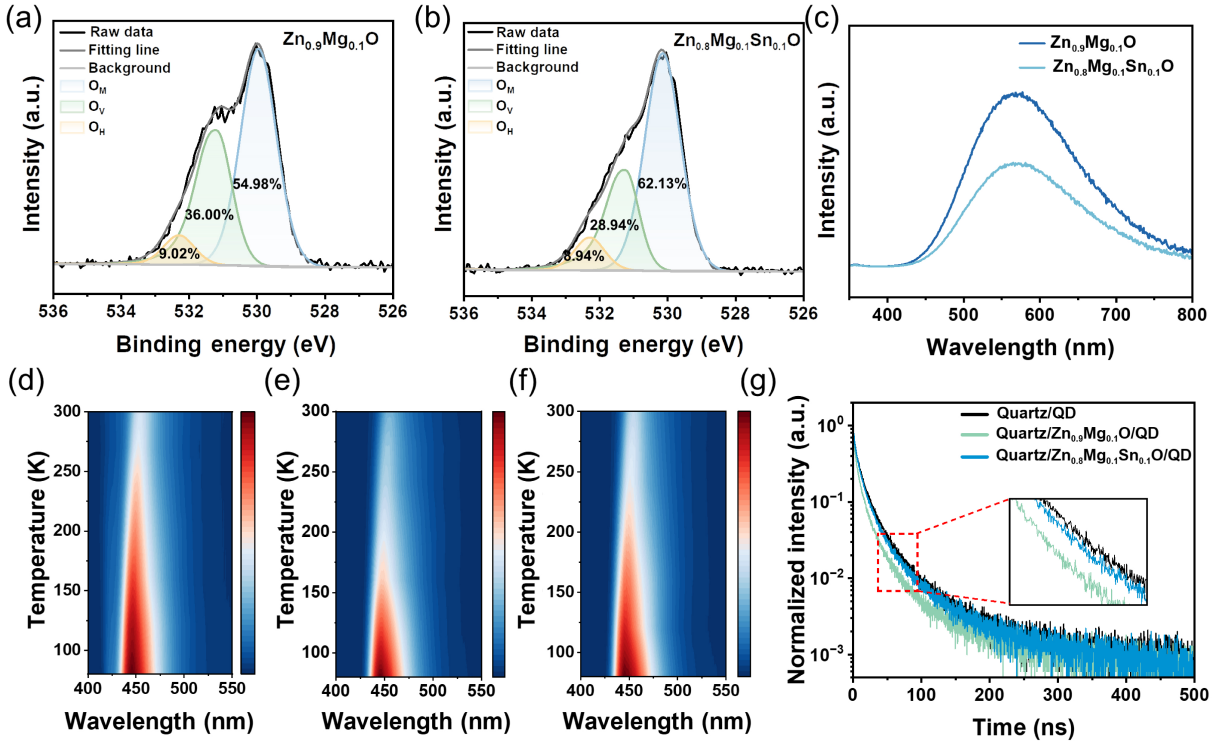

Figure 2 O 1s XPS spectra of (a) $Zn_{0.9}Mg_{0.1}O$ and (b) $Zn_{0.8}Mg_{0.1}Sn_{0.1}O$. (c) PL spectra of $Zn_{0.9}Mg_{0.1}O$ and $Zn_{0.8}Mg_{0.1}Sn_{0.1}O$ films. Evolution of temperature-dependent PL properties of blue QDs fabricated on (d) Quartz, (e) Quartz/$Zn_{0.9}Mg_{0.1}O$, and (f) Quartz/$Zn_{0.8}Mg_{0.1}Sn_{0.1}O$ substrates, respectively. (g) TRPL characteristics of blue QD films on different substrates.

and QDs/$Zn_{0.8}Mg_{0.1}Sn_{0.1}O$ remained significantly higher at high temperatures, retaining 74% and 84% of their initial intensity, respectively. This improvement suggests effective defect passivation in $Zn_{0.8}Mg_{0.1}Sn_{0.1}O$, which suppresses detrimental interactions at the QD/ETL interface. This trend is consistent with the PL quantum yield (PLQY) results shown in Fig. S9 in the ESM.

To verify this defects passivation effect, we further performed the time-resolved PL (TRPL) measurements to get insight into the interfacial exciton behavior at QD/$Zn_{0.9}Mg_{0.1}O$ or QD/$Zn_{0.8}Mg_{0.1}Sn_{0.1}O$ interface (Fig. 2(g)). The exciton lifetimes were fitted by a bi-exponential model, where the fast decay process of nonradiative recombination (τ_1) was associated with the quenching of free carriers at the interface, and the slow decay process of radiative recombination (τ_2) was related to the radiative recombination (summarized in Table S2 in the ESM). It is revealed that the nonradiative recombination ratio increases significantly for $Zn_{0.9}Mg_{0.1}O$/QDs (Fig. S10 in the ESM), and the τ_{ave} is reduced to 11.18 ns, which is believed to be associated with a spontaneous Förster resonant energy transfer (FRET) or charge trapping. In contrast, the exciton lifetime of $Zn_{0.8}Mg_{0.1}Sn_{0.1}O$/QD (15.32 ns) was enhanced closed to QD (16.63 ns), firmly proving the inhibited interfacial exciton quenching for strengthened radiative recombination.

2.3 Electrical properties of ZMO and ZMSO ETLs

Regarding the electrochemical properties, the Sn doping strategy will also affect the energy-level alignment and electrical transport characteristics of ETLs. In order to investigate the influence of Sn doping on the energy levels and optical properties, we analyzed the ultraviolet photoelectron spectroscopy (UPS) and ultraviolet–visible (UV–Vis) absorption spectra of $Zn_{0.9}Mg_{0.1}O$ and $Zn_{0.8}Mg_{0.1}Sn_{0.1}O$ films. Figures 3(a) and 3(b) display the secondary electron cut-off ($E_{cut\text{-}off}$) region and the starting valence band edge region ($E_{on\text{-}sent}$), and the valence band maximum (VBM) energy levels were calculated to be 6.94 and 6.69 eV respectively by the equation VBM = 21.2 eV − ($E_{cot\text{-}off}$ − E_{onsest}). Additionally, the Tauc plots from UV–Vis absorption spectra, indicate bandgap of 3.57 and 3.50 eV (Fig. S11 in the ESM). The corresponding conduction band minimum (CBM) energy levels were then calculated as −3.37 eV ($Zn_{0.9}Mg_{0.1}O$) and −3.19 eV ($Zn_{0.8}Mg_{0.1}Sn_{0.1}O$), and detailed information is recorded in the Table S3 in the ESM. These findings indicate that Sn doping leads to up-shifted CBM energy level, thus increasing energy barrier for electron transport at the ETL/Al interface and impeding excessive electron injection (Fig. 3(c)).

To further investigate the electron injection and transport capabilities of $Zn_{0.9}Mg_{0.1}O$ and $Zn_{0.8}Mg_{0.1}Sn_{0.1}O$ ETLs, electron-only device (EOD) with the structure of indium tin oxide (ITO)/QD/ZMO or ZMSO/Al were fabricated. Correspondingly, hole-only devices (HODs) with the layer structures as ITO/PEDOT:PSS/TFB/QDs/MoO_3/Al were also fabricated. The current densities versus driving voltage are presented in Fig. 3(d). The electron current in $Zn_{0.8}Mg_{0.1}Sn_{0.1}O$-based EODs decreased by an order of magnitude, much closer to the hole current compared with $Zn_{0.9}Mg_{0.1}O$-based devices, which resulted in facilitated charge balance in the QLEDs. Furthermore, the charge mobilities of TFB and ZMSO were measured through the space charge-limit-current (SCLC) technique, as seen in Fig. S12 in the ESM. The results show that the electron mobility of ZMSO continuously decreases with the increase of Sn doping ratio, with values of 1.7×10^{-3} $cm^2 \cdot V^{-1} \cdot s^{-1}$ ($Zn_{0.9}Mg_{0.1}O$), 6.08×10^{-4} $cm^2 \cdot V^{-1} \cdot s^{-1}$ ($Zn_{0.85}Mg_{0.1}Sn_{0.05}O$), 3.19×10^{-4} $cm^2 \cdot V^{-1} \cdot s^{-1}$ ($Zn_{0.8}Mg_{0.1}Sn_{0.1}O$), and 9.04×10^{-5} $cm^2 \cdot V^{-1} \cdot s^{-1}$ ($Zn_{0.75}Mg_{0.1}Sn_{0.15}O$), respectively. It should be noted that excessive Sn

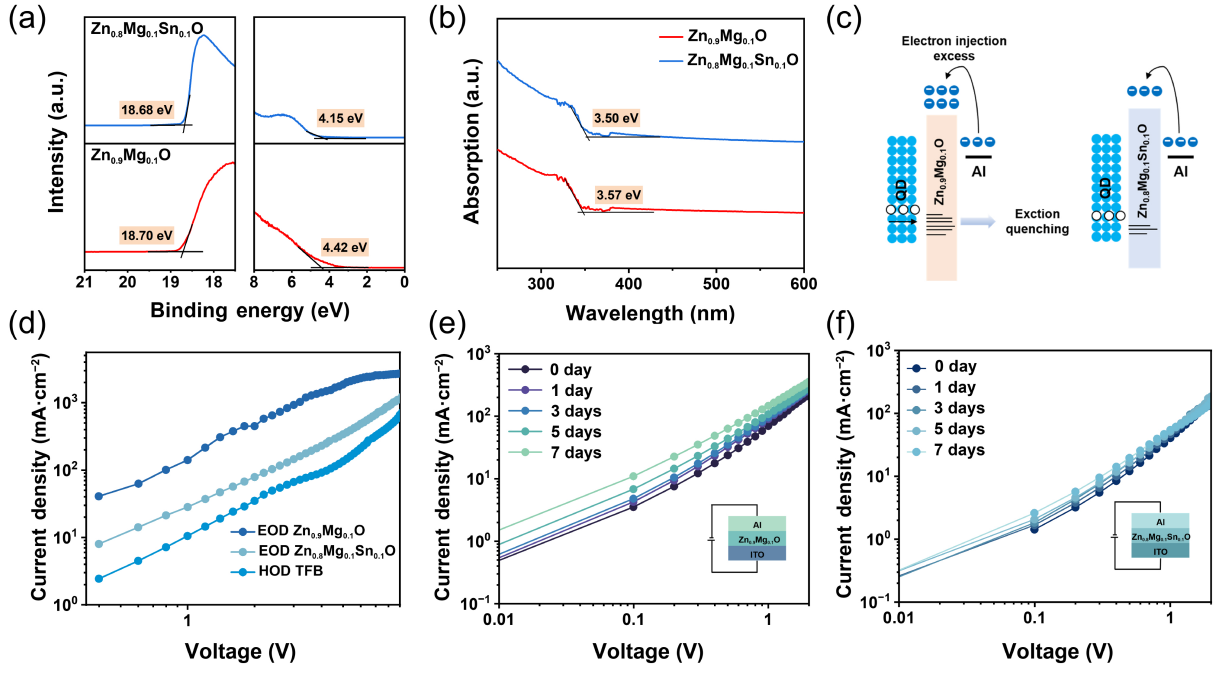

Figure 3 (a) UPS and (b) UV–Vis absorption spectra of ZMO and ZMSO films. (c) Schematic diagram of electron transport and interfacial exciton quenching at the QD/ETL interface. (d) *J*–*V* characteristic of EOD and HOD devices. (e) and (f) *J*–*V* characteristic of devices glass/ITO/ZMO or ZMSO/Al during storage, the insets illustrate the device structures.

doping (15%) leads to a significant decrease in electron mobility, which is seriously mismatched with the mobility of TFB (3.08×10^{-4} $cm^2 \cdot V^{-1} \cdot s^{-1}$), thus affects the hole-electron injection balance.

Next, we conducted additional time-dependent EOD experiments to compared the electronic stabilities of $Zn_{0.9}Mg_{0.1}O$ and $Zn_{0.8}Mg_{0.1}Sn_{0.1}O$. Both devices were fabricated using the same structure of ITO/ETL (50 nm)/Al and encapsulated with the same resin. The *J*–*V* characteristics are shown in Figs. 3(e) and 3(f). Meanwhile, we compared the decline degree of the voltages of ZMO- and ZMSO-based EODs over time at a current of 100 $mA \cdot cm^{-1}$, as shown in Fig. S13 in the ESM. After storage for 0–7 days, the voltage of the $Zn_{0.8}Mg_{0.1}Sn_{0.1}O$-based device remained slightly changed (~ 9% decline), whereas that of ZMO changed significantly (~ 41% decline). As reported in previous studies, this change in curves is attributed to the chemical reaction of resin acid at the ETL and ETL/Al interface. Obviously, ZMSO-based EOD exhibit superior electronic stability due to the enhanced chemical inertness induced by Sn doping, contributing to improving the storage stability of the QLEDs.

2.4 Enhancements in QLED efficiency and stability

To further investigate the effect of ZMSO ETLs on the performance of QLEDs, we fabricated all spin-coated blue QLEDs following the configuration in Fig. 4(a). The device structure was ITO (110 nm)/PEDOT:PSS (32 nm)/HTLs (20 nm)/QDs (20 nm)/ZMSO or ZMO (50 nm)/Al (100 nm), with fabrication details provided in the Experimental section. In this device, The emissive layer consisted of blue QDs with a ZnSeTe-ZnS core–shell structure, whose absorption and PL spectra are shown in Fig. S14 in the ESM. PEDOT:PSS and TFB served as the hole injection layer and hole transport layer, respectively. The energy level diagram of the device is illustrated in Fig. 4(b).

First, a series of ZMSO ETLs with different Sn molar ratios (0%, 5%, 10%, and 15%) were investigated to ascertain the best ratio. Here, Mg molar ratio was fixed at 10%, which is the commonly used doping ratio as in previous reports. The relevant electroluminescence (EL) spectra, current density–luminance–voltage (*J*–*L*–*V*), current efficiency–luminance (CE–*L*), power efficiency–luminance (PE–*L*) and EQE–luminance (EQE–*L*) characteristics of devices are presented in Figs. 4(c)–4(f), and the detailed device performances are summarized in Table S4 in the ESM. It can be seen that the normalized EL spectra of these devices kept almost unchanged with pure blue emission at 456 nm and a FWHM of 30 nm (Fig. 4(c)), indicating that Sn doping ETLs will not change the exciton recombination zone. The inset of Fig. 4(c) shows photos of QLEDs operating at 3 V, corresponding to the CIE 1931 coordinates of (0.14, 0.11) (Fig. S15 in the ESM). Additionally, the device performances gradually improved as the Sn ratio increased from 0% to 10%, then declined with further increased ratio. The optimal performance was attained with doping ratio of 10%, where the device exhibited best EQE of 19.7%, with 17.0 $cd \cdot A^{-1}$ for CE and 17.8 $lm \cdot W^{-1}$ for PE, compared to 9.6% (9.6 $cd \cdot A^{-1}$, 10.0 $lm \cdot W^{-1}$) for ZMO-based control devices. It is worthy to note that $Zn_{0.8}Mg_{0.1}Sn_{0.1}O$-based QLEDs not only exhibited higher peak EQE but also lower efficiency roll-off (~ 31.2% at 10,000 $cd \cdot m^{-2}$), whereas $Zn_{0.9}Mg_{0.1}O$-based devices suffered a severe 69.3% roll-off. The best device performance based on 10% Sn doping ratio of ZMSO is mainly attributed to its low defect state and appropriate electron injection and transport capabilities.

Furthermore, a comparison was made between two groups of blue QLEDs utilizing OP- and MF-synthesized $Zn_{0.8}Mg_{0.1}Sn_{0.1}O$ ETLs in terms of device reproducibility. Here, we synthesized 20 batches of ZMSO NCs by each method, and fabricated corresponding devices from the different NC batches (Fig. S16 in the ESM). As shown in Fig. 4(g), MF-based devices exhibited superior reproducibility of device performance, demonstrating average peak external quantum efficiencies (EQEs) of 18.3% (from

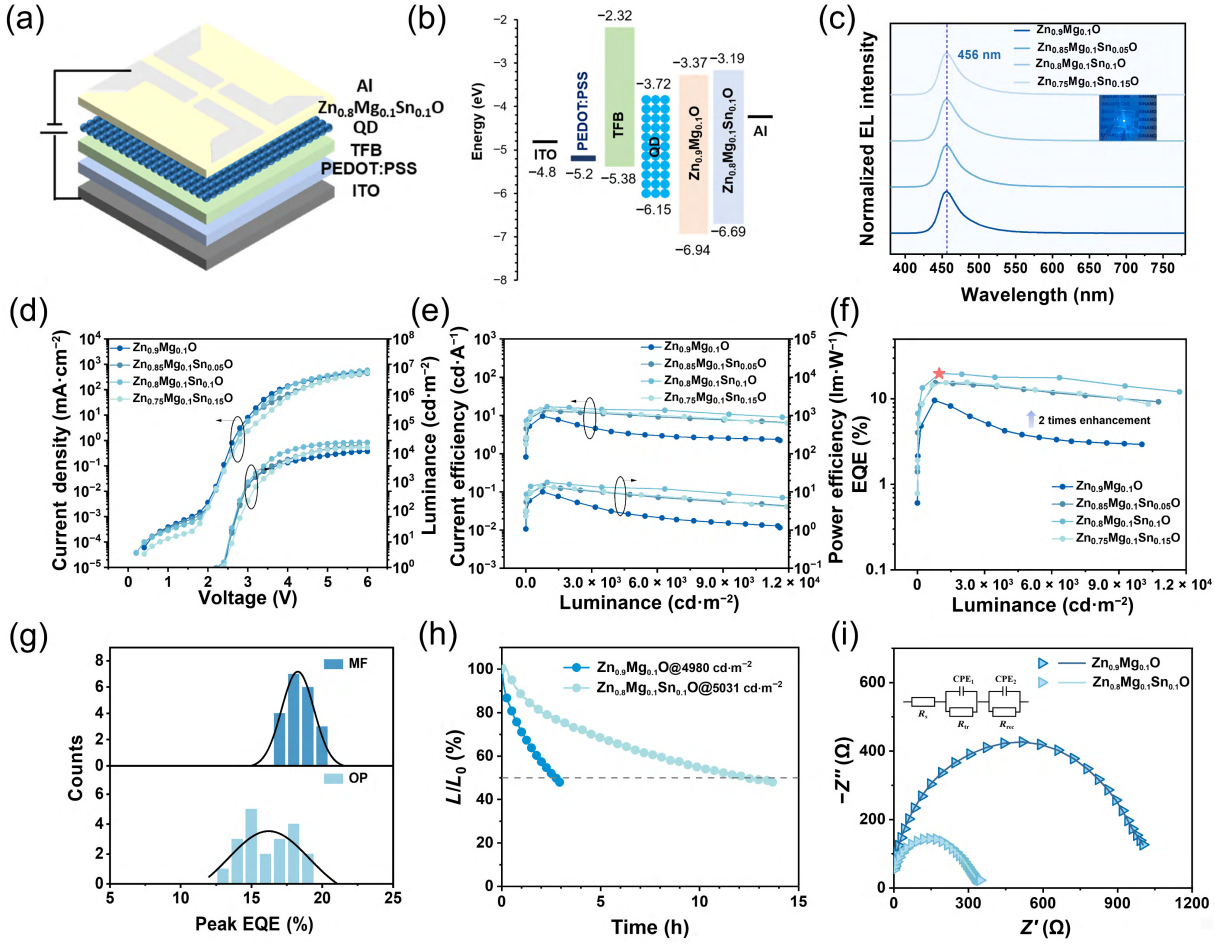

Figure 4 (a) Diagram of QLED structure. (b) Energy levels of the functional layers of blue QLED. (c) EL spectra (inset: blue emitting photographs). (d) *J*–*L*–*V*. (e) CE–PE–*L* and (f) EQE–*L* characteristics of the blue devices with different ETLs. (g) Histogram of peak EQEs of ZMSO NCs from 20 devices syntheized by MF and OP respectively. (h) Lifetime of device with different ETLs. (i) Nyquist plots of EIS spectra of blue QLEDs and their fitting curves.

16.64% to 19.71%, standard deviation: 0.92) comparing to 16.2% (from 12.89% to 19.06%, standard deviation: 1.62) for OP-based devices. Although OP- and MF-based $Zn_{0.8}Mg_{0.1}Sn_{0.1}O$ have similar photoelectric characteristics (Fig. S17 in the ESM), the MF reaction ensured the batch stability of NC synthesis, thereby enhanced the reproducibility and stability of device fabrication.

Regarding the device stability, the half lifetime T_{50} (the time required for the initial luminance (L_0 ~ 5000 cd·m^{-2}) to decrease to 50%) of ZMO- and ZMSO-based QLEDs were 2.74 and 12.41 h respectively (Fig. 4(h)). Using the formula (an acceleration factor of 1.86) to convert T_{50} at L_0 of 100 cd·cm^{-2}, the device lifetime was extended from 3931 h for the control ZMO-based devices to 18,236 h for ZMSO-based devices with a 4.6-fold improvement. Among them, non-radiative Joule heating was identified as the primary degradation mechanism. Therefore, the Joule heat generated during device operation was measured to assess the inhibition effect of ZMSO ETL on non-radiative recombination. Figure 5(a) shows the monitored real-time temperature of QLEDs based on ZMO ETL and ZMSO ETL using an infrared camera. The surface temperature of the QLEDs device after operating for 2 min was recorded at different luminance under room temperature condition. For the control QLEDs (ZMO ETL), the surface temperature increased by 28.6 °C as luminance increased from 0 to 10,000 cd·m^{-2}. This significant increase in surface temperature is attributed to the significant Joule heat generation during device operation. In contrast, ZMSO-based QLEDs exhibited a smaller temperature increase of only 13.8 °C over the same luminance range. The heat generation rate and value are significantly suppressed, especially at high luminance. The reduction of heat generated during device operation indicates that the Sn doping into ZMO effectively reduces the non-radiative recombination ratio in the device.

To find out the mechanism of device performance improvement, electrochemical impedance spectroscopy (EIS) measurements were carried out at a forward bias of 3 V. Figure 4(i) presents the Nyquist plots, fitted using a simplified resistance-capacitance (RC) circuit. The fitting results are shown in Table S5 in the ESM Obviously, the recombination resistance (R_{rec}) of ZMSO-based device is lower than that of the control ZMO device, indicating a higher recombination rate. That is to say, the hole–electron recombination probability promotes significantly on the ZMSO-based device. Therefore, the appropriate band structure and reduced crystal defects of ZMSO mitigate interface charge accumulation and exciton quenching, further promoting effective exciton recombination inside the device.

In multicolor pixel displays, the shelf-stability of devices is also a very important indicator, i.e., the performance of the devices should not change significantly over storage time, which are critical for practical applications. Therefore, we investigated the change of performance for the ZMSO- and ZMO-based QLEDs at different times within seven days (Figs. S18 and S19 in the ESM). The

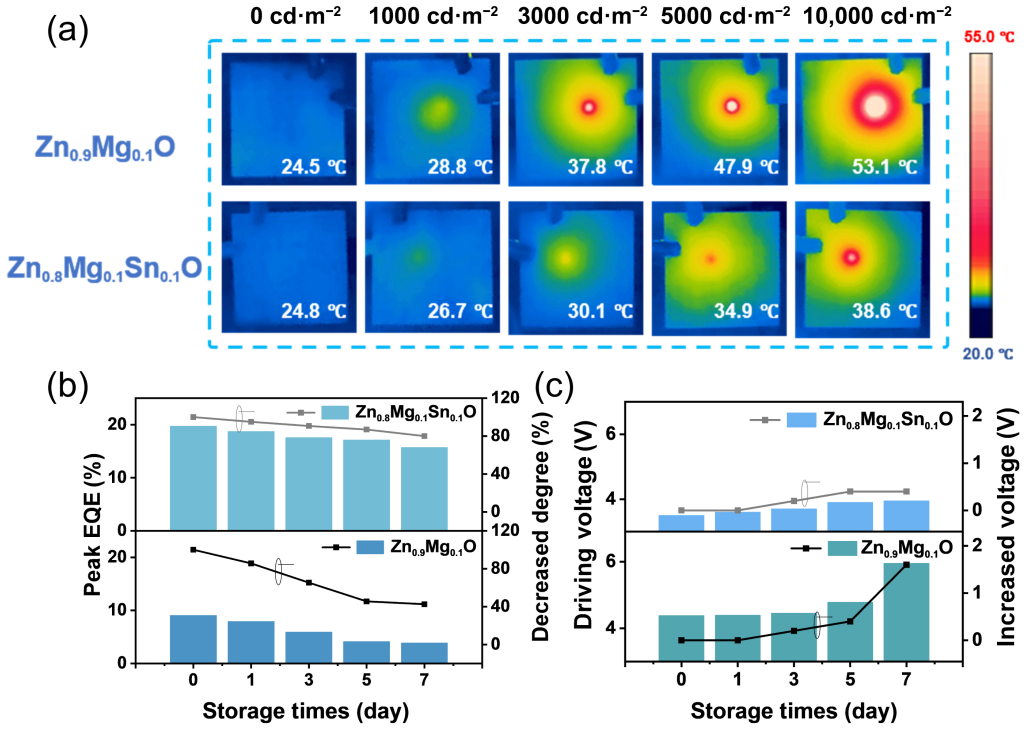

Figure 5 (a) Surface temperature of the device under different brightness, with the brightness operating for 2 min. Evolutions of (b) peak EQE and (c) driving voltage of ZMO or ZMSO based QLED @5000 cd·m^{-2} during storage.

corresponding characteristics include the changes of peak EQEs and driving voltages (5000 cd·m^{-2}) are shown in Figs. 5(b) and 5(c), respectively. After storage for seven days, both devices showed varying degrees negative ageing. The negative ageing is characterized by the decrease of EQEs and the increase of driving voltages. The ZMO-based device showed significant degradation, with 57.4% drop in peak EQE and 1.6 V increase in driving voltage. In contrast, the ZMSO-based device exhibited high shelf-stabilities, with minimal changes in these parameters (20.4% drop for EQE, 0.4 V increase for voltage), which is attributed to the enhanced chemical stabilities induced at ZMSO/Al interface.

3 Conclusion

In summary, we successfully synthesized high-quality Sn^{4+}/Mg^{2+} co-doped ZnO (i.e., ZMSO) NCs in a MF reactor, with consistent production reproducibility, reduced trap states, favorable energy band, as well as structural and electrical stability. Based on the high-quality ZMSO ETLs, the interfacial exciton quenching and excess electron injection have been inhibited while the film quality and chemical stability have been improved. Consequently, the overall performance of ZMSO-based blue ZnSeTe QLEDs have been improved significantly and EQE of 19.7% has been achieved, which is 2-fold increase comparing to that of the control ZMO device (9.6%), and 4.6-fold improvement in lifetime (@100 cd·m^{-2}) from 3931 to 18,236 h. Furthermore, the ZMSO-based QLED demonstrated exceptional stability of shelf life. The present work provided promising potential for the commercialization of QLEDs in future.

4 Experimental section

All solvents and materials were used as received from commercial sources without further purification. ZnSeTe-ZnS core–shell blue QDs with an absolute fluorescence quantum yield (PL QY) of roughly 66% and a spectral bandwidth of 26 nm at the 453 nm emission peak were provided by Mesolight (China). Zinc acetate dihydrate ($Zn(OAc)_2{\cdot}2H_2O$) was purchased from Alfa Aesar. Tin(IV) acetate ($Sn(OAc)_4$) and magnesium acetate tetrahydrate ($Mg(OAc)_2{\cdot}4H_2O$) were purchased from Sigma-Aldrich. Tetramethylammonium hydroxide (TMAH) was purchased from J&K Scientific Ltd. Ethyl acetate, ethanol, and dimethyl sulfoxide (DMSO) were purchased from Sinopharm Chemical Reagent Co., Ltd.

Synthesis of ZMO and ZMSO NC: As illustrated in Fig. 1(a), ZMSO NCs were synthesized using a MF reactor. All operations were conducted in a nitrogen-filled glove box (O_2 < 0.1 ppm, H_2O < 0.1 ppm). $Zn(OAc)_2{\cdot}2H_2O$, $Sn(OAc)_4$, and $Mg(OAc)_2{\cdot}4H_2O$ were separately dissolved in DMSO (0.1 mol·L^{-1}), these solutions were blended at specific molar ratios to obtain precursor solution A (the molar fraction of Sn element was accurately adjusted to 0%, 5%, 10%, and 15% in the respective samples), while TMAH in ethanol (0.5 mol·L^{-1}) served as precursor solution B. These solutions were infused into the MF reactor at 3 mL·min^{-1} (precursor solution A) and 2 mL·min^{-1} (precursor solution B), reacting at 30 °C for 10 min. The product was precipitated with excess ethyl acetate (2 h), centrifuged at 3000 rpm for 5 min (repeated 3 times with supernatant removal), and redispersed in ethanol (30 mg·mL^{-1}) for storage at 4 °C. The ZMO NCs were synthesized under identical conditions for comparison. We also synthesized ZMO and ZMSO NCs with the traditional OP method as in previous reports.

Fabrication of blue QLEDs: ITO glass substrates were ultrasonically cleaned in isopropanol and deionized water for 15 min each before use, followed by UV-ozone treatment for 20 min. Poly(3,4-ethylenedioxythiophene):poly(styrenesulfonate) (PEDOT:PSS) was spin-coated in air at 4000 rpm for 40 s and

annealed on a hotplate at 130 °C for 15 min. The ITO glass was then transferred into an N_2 glovebox (H_2O < 1 ppm, O_2 < 1 ppm). A second layer of poly(9,9-dioctylfluorene-co-bis(4-butylphenyl) diphenylamine) (TFB, chlorobenzene, 8 mg·mL^{-1}) was spin-coated onto the pre-deposited PEDOT:PSS layer at 3000 rpm for 30 s and annealed at 130 °C for 15 min. Subsequently, the QD layer (octane, 15 mg·mL^{-1}) and ZMSO nanocrystals (NCs, in ethanol, 30 mg·mL^{-1}) were sequentially spin-coated at 3000 rpm for 30 s each, followed by annealing at 100 °C for 1 min and 90 °C for 15 min, respectively. Finally, the samples were transferred to a vacuum chamber where a 50 nm thick aluminum cathode was deposited (rate: 2 Å·s^{-1}). The devices were then encapsulated using UV-curable resin.

Characterizations: All tests and optical measurements were performed under ambient conditions. XPS analysis was performed using a Thermo Scientific K-Alpha spectrometer to confirm the successful incorporation of Sn^{4+}. UPS analysis was conducted with an unfiltered HeI (21.22 eV) gas discharge lamp, and a sample bias of 10 V was applied to observe the secondary electron cutoff (SEC) of ZMSO NCs on PHI 5000 Versaprobe II @Nano-X, SINANO. XRD analysis was conducted on a Rigaku Ultimate IV diffractometer (Rigaku, Japan) to reveal the effect of Sn^{4+} doping on the crystal structure. The size distribution of ZMSO NCs was measured using a Malvern Zetasizer series instrument. The surface roughness of ZMSO NC thin films was characterized by AFM using a Dimension ICON microscope. UV–Vis absorption spectra were collected using a PerkinElmer Lambda 750 UV/Vis spectrophotometer to determine the band gap. PL measurements were performed using a 400 nm He-Cd laser to characterize the optical properties of the synthesized NCs. To investigate the quenching effect of interfacial excitons at the ETL/QD interface, TRPL decay curves of samples on quartz/QD and quartz/ZMSO or ZMO/QD were measured using an Edinburgh Instruments FLS1000 spectrometer. *J*–*L*–*V*, CE–*L*, power efficiency-luminance (PE–*L*), and EQE–*L* curves were characterized using a computer-controlled Keithley 2400 Sourcemeter. The active device area was 2 mm × 2 mm for all devices, and only the luminance in the forward direction was measured during testing.

Electronic Supplementary Material: Supplementary material (size distribution, AFM images, XRD analysis, XPS spectra, PL characteristics, PLQY, Tauc diagram, *J*–*V* characteristic, CIE 1931, and devices characteristics) is available in the online version of this article at https://doi.org/10.26599/NR.2026.94908518.

Data availability

All data needed to support the conclusions in the paper are presented in the manuscript and the Electronic Supplementary Material. Additional data related to this paper may be requested from the corresponding author upon request.

Acknowledgements

This work is financially supported by the National Key Research and Development Program of China (No. 2022YFB3606500), the National Natural Science Foundation of China (No. 62504241), the Postdoctoral Fellowship Program of CPSF (No. GZC20250385), the China Postdoctoral Science Foundation (No. 2025M770157), the Jiangsu Provincial Frontier Technology R&D Program (No. BF2024034), Funded by Basic Research Program of Jiangsu (No. BK20250508), and the Jiangsu Funding Program for Excellent Postdoctoral Talent (No. 2025ZB472). The authors are grateful for the technical support for Nano-X from Suzhou Institute of Nano-Tech and Nano-Bionics, Chinese Academy of Sciences (No. SINANO).

Declaration of competing interest

All the contributing authors report no conflict of interests in this work.

Author contribution statement

C. R. D.: Data curation, validation, writing manuscript. L. M. X.: Data curation, project administration, validation, writing manuscript, experimental design. W. F. W.: Data curation, formal analysis. T. W.: Data curation, formal analysis. Y.-Q.-Q. Y.: Data curation, validation. J. Y. Z.: Formal analysis, investigation. X. Q. M.: Formal analysis, investigation. W. M. S.: Conceptualization, project administration, resources, writing – review & editing. T. Z. Y.: Conceptualization, writing – review & editing. Z. C.: Writing review. All the authors have approved the final manuscript.

Use of AI statement

None.

References

[1] Fan, J. P.; Han, C. F.; Yang, G. J.; Song, B.; Xu, R.; Xiang, C. Y.; Zhang, T.; Qian, L. Recent progress of quantum dots light-emitting diodes: Materials, device structures, and display applications. *Adv. Mater.* **2024**, *36*, 2312948.

[2] Kim, J.; Roh, J.; Park, M.; Lee, C. Recent advances and challenges of colloidal quantum dot light-emitting diodes for display applications. *Adv. Mater.* **2024**, *36*, 2212220.

[3] Dai, X. L.; Deng, Y. Z.; Peng, X. G.; Jin, Y. Z. Quantum-dot light-emitting diodes for large-area displays: Towards the dawn of commercialization. *Adv. Mater.* **2017**, *29*, 1607022.

[4] Xiao, Z.; Zhang, M.; Ding, Y. H.; Shi, Z. Y.; Yin, Z. H.; Deng, H. H.; Meng, L. L.; Xu, B. J.; Liu, H. Solution-processed quantum dot micropatterns: From liquid manipulation to high-performance quantum dot light-emitting diode devices. *ACS Nano* **2025**, *19*, 10609–10619.

[5] Yuan, Q. L.; Wang, T.; Yu, P. L.; Zhang, H. Z.; Zhang, H.; Ji, W. Y. A review on the electroluminescence properties of quantum-dot light-emitting diodes. *Org. Electron.* **2021**, *90*, 106086.

[6] Yu, Y.; Liang, Y.; Yong, J.; Li, T. Z.; Hossain, M. S.; Liu, Y. T.; Hu, Y. H.; Ganesan, K.; Skafidas, E. Low-temperature solution-processed transparent QLED using inorganic metal oxide carrier transport layers. *Adv. Funct. Mater.* **2022**, *32*, 2106387.

[7] Zhang, W. D.; Ding, S. H.; Zhuang, W. D.; Wu, D.; Liu, P.; Qu, X. W.; Liu, H. C.; Yang, H. C.; Wu, Z. H.; Wang, K. et al. InP/ZnS/ZnS core/shell blue quantum dots for efficient light-emitting diodes. *Adv. Funct. Mater.* **2020**, *30*, 2005303.

[8] Han, C. F.; Qian, R. X.; Xiang, C. Y.; Qian, L. Materials and device engineering to achieve high-performance quantum dots light emitting diodes for display applications. *Chin. Phys. B* **2023**, *32*, 128506.

[9] Chen, Z.; Tian, N. F.; Chen, X. H.; Zhang, Y.; Liu, B. C.; Yuan, Z. L.; He, C. Y.; Wang, A. J.; Li, Y.; Ren, S. M. et al. Large scale synthesis of red-emitting quantum dots for efficient and stable light-emitting diodes. *Adv. Mater.* **2025**, *37*, 2413978.

[10] Liu, Y. T.; Sun, Y. Y.; Yan, X. H.; Li, B.; Wang, L.; Li, J. S.; Sun, J. H.; Guo, Y. Q.; Liu, W. P.; Hu, B. B. et al. Realizing low voltage-driven bright and stable quantum dot light-emitting diodes through energy landscape flattening. *Light: Sci. Appl.* **2025**, *14*, 50.

[11] Vasan, R.; Gao, F.; Manasreh, M. O.; Heyes, C. D. All-inorganic QLEDs utilizing resonant energy transfer between non-stoichiometric nickel oxide hole transport layer and alloyed CdSe/ZnS quantum dots. *J. Mater. Sci.: Mater. Electron.* **2025**, *36*, 1190.

[12] Wang, Z. N.; Sun, Y.; Yao, W. B.; Ba, Q.; Wang, H. Effects of cadmium exposure on the immune system and immunoregulation. *Front. Immunol.* **2021**, *12*, 695484.

[13] Won, Y. H.; Cho, O.; Kim, T.; Chung, D. Y.; Kim, T.; Chung, H.; Jang, H.; Lee, J.; Kim, D.; Jang, E. Highly efficient and stable InP/ZnSe/ZnS quantum dot light-emitting diodes. *Nature* **2019**, *575*, 634–638.

[14] Hajeb, P.; Sloth, J. J.; Shakibazadeh, S.; Mahyudin, N. A.; Afsah-Hejri, L. Toxic elements in food: Occurrence, binding, and reduction approaches. *Compr. Rev. Food Sci. Food Saf.* **2014**, *13*, 457–472.

[15] Su, Y. Y.; Hu, M.; Fan, C. H.; He, Y.; Li, Q. N.; Li, W. X.; Wang, L. H.; Shen, P. P.; Huang, Q. The cytotoxicity of CdTe quantum dots and the relative contributions from released cadmium ions and nanoparticle properties. *Biomaterials* **2010**, *31*, 4829–4834.

[16] Channa, A. I.; Bai, S.; Wang, Z. M.; Tong, X. Advancements in eco-friendly colloidal quantum dots and their application in light emitting diodes: Achieving bright and color-pure emission for displays. *Laser Photon. Rev.* **2025**, *19*, 2400678.

[17] Chen, Z. N.; Li, H. T.; Yuan, C. X.; Gao, P. L.; Su, Q.; Chen, S. M. Color revolution: Prospects and challenges of quantum-dot light-emitting diode display technologies. *Small Methods* **2024**, *8*, 2300359.

[18] Li, H.; Zhang, J. Y.; Wen, W.; Zhao, Y. Y.; Gao, H. F.; Ji, B. Q.; Wang, Y. J.; Jiang, L.; Wu, Y. C. Highly efficient light-emitting diodes via self-assembled InP quantum dots. *Nat. Commun.* **2025**, *16*, 4257.

[19] Bian, Y. Y.; Yan, X. H.; Chen, F.; Li, Q.; Li, B.; Hou, W. J.; Lu, Z. Z.; Wang, S. B.; Zhang, H.; Zhang, W. J. et al. Efficient green InP-based QD-LED by controlling electron injection and leakage. *Nature* **2024**, *635*, 854–859.

[20] Wu, Q. Q.; Cao, F.; Yu, W. K.; Wang, S.; Hou, W. J.; Lu, Z. Z.; Cao, W. R.; Zhang, J. Q.; Zhang, X. Y.; Yang, Y. G. et al. Homogeneous ZnSeTeS quantum dots for efficient and stable pure-blue LEDs. *Nature* **2025**, *639*, 633–638.

[21] Huang, Y. J.; Cao, S.; Liang, Y.; Li, Q. Y.; Chen, Z. T.; Lai, C. L.; Zou, B. S.; Zhao, J. L. High-efficiency and stable ZnSeTe-based blue QLEDs enabled by freeze-dried SnO_2 nanoparticle interlayers. *Laser Photon. Rev.* **2025**, *19*, 2500049.

[22] Liu, Y.; Jiang, C. B.; Song, C.; Wang, J. H.; Mu, L.; He, Z. W.; Zhong, Z. J.; Cun, Y.; Mai, C.; Wang, J. et al. Highly efficient all-solution processed inverted quantum dots based light emitting diodes. *ACS Nano* **2018**, *12*, 1564–1570.

[23] Guan, Z. Y.; Huang, Y.; Wang, Z. J.; Sun, J. Y.; Shan, C. W.; Xu, Y. G.; Wu, D.; Tang, A. W.; Sun, X. W.; Wang, K. Surface defects passivation of ZnSeTe/ZnSe/ZnS quantum dots by iodine ions for highly efficient blue light-emitting diodes. *Adv. Opt. Mater.* **2024**, *12*, 2401884.

[24] Kim, Y. H.; Yoon, S. Y.; Yang, H. Blue-emissive ZnSeTe quantum dots and their electroluminescent devices. *J. Phys. Chem. Lett.* **2024**, *15*, 2142–2151.

[25] Lee, S. H.; Song, S. W.; Yoon, S. Y.; Jo, D. Y.; Kim, S. K.; Kim, H. M.; Kim, Y.; Park, S. M.; Yang, H. Heterostructural tailoring of blue ZnSeTe quantum dots toward high-color purity and high-efficiency electroluminescence. *Chem. Eng. J.* **2022**, *429*, 132464.

[26] Zhang, W. J.; Li, B.; Chang, C.; Chen, F.; Zhang, Q.; Lin, Q. L.; Wang, L.; Yan, J. H.; Wang, F. F.; Chong, Y. H. et al. Stable and efficient pure blue quantum-dot LEDs enabled by inserting an anti-oxidation layer. *Nat. Commun.* **2024**, *15*, 783.

[27] Zhao, J.; Wang, L.; Lv, P.; Wang, F.; Li, X.; Chen, S.; Qian, L.; Tang, A. Performance enhancement of cadmium-free quantum-dot light-emitting diodes via Cl-passivated $Zn_{1-x-y}Sn_xMg_yO$ nanoparticles as electron transport layers. *Laser Photon. Rev.* **2023**, *17*, 2200749.

[28] Ghorbani, A.; Aziz, H. Progressive quenching of luminescence from quantum dot thin films in proximity with ZnMgO in unencapsulated stacks. *Org. Electron.* **2024**, *131*, 107087.

[29] Kim, J. Recent progresses and challenges in colloidal quantum dot light-emitting diodes: A focus on electron transport layers with metal oxide nanoparticles and organic semiconductors. *Nanoscale Horiz.* **2024**, *9*, 2167–2197.

[30] Guo, Y.; Liu, B. C.; Chen, Z.; Song, W. D.; Tian, N. F.; Wu, W. H.; Fan, X. K.; Zhan, Y. F.; Meng, F. Y.; Zeng, Q. G. et al. Water-passivated ZnMgO nanoparticles for blue quantum dot light-emitting diodes. *J. Mater. Chem. C* **2021**, *9*, 10381–10387.

[31] Coke, M. L.; Kennedy, O. W.; Sagar, J. T.; Warburton, P. A. Electron confinement at diffuse ZnMgO/ZnO interfaces. *APL Mater.* **2017**, *5*, 016102.

[32] Yang, M.; Bao, H.; Jing, Y. Y.; Ao, Z. T.; Wang, J.; Wu, L. J.; Feng, Y. B.; Song, T. L.; Wu, X. G.; Yan, Y. R. et al. Siloxane-modified ZnMgO nanoparticles with enhanced colloidal stability and improved quantum dot light-emitting diode stability. *J. Phys. Chem. Lett.* **2025**, *16*, 2764–2770.

[33] Feng, Y. B.; Krasnov, P.; Yang, M.; Li, M. L.; Boldyreva, A.; Boldyrev, K.; Ju, Y. Y.; Zhong, H. Z. Gas-initiated chemical alterations in ZnMgO electron transport layer: Key gas instability drivers in quantum-dot light-emitting diodes. *Nano Res.* **2025**, *18*, 94907649.

[34] Shi, H. F.; Ren, Z. W.; Zheng, Z. Y.; Zhou, X.; Luo, C. Z.; Ji, H. F.; Zhang, Y. Z.; Chen, H.; Wu, C. L.; Chen, Y. Mercaptopropionic acid capped ZnMgO for efficient and stable quantum dot light-emitting diodes. *Laser Photon. Rev.* **2024**, *18*, 2400473.

[35] Su, Q.; Sun, Y. Z.; Zhang, H.; Chen, S. M. Origin of positive aging in quantum-dot light-emitting diodes. *Adv. Sci.* **2018**, *5*, 1800549.

[36] Sun, C. Y.; Li, Q. Y.; Cao, S.; Wang, Y. J.; Zou, B. S.; Zhao, J. L. Synergistic chloride passivation and inorganic shell confinement in ZnMgO nanoparticles for efficient and stable blue ZnSeTe QLEDs. *J. Phys. Chem. Lett.* **2025**, *16*, 5441–5448.

[37] Yoon, S. Y.; Kim, Y. H.; Lee, S. H.; Yang, H.; Jo, D. Y.; Kim, H. M.; Kim, Y.; Park, S. M.; Choi, S. W.; Yang, H. Efficient, stable blue light-emitting diodes enabled by heterostructural alteration of ZnSeTe quantum dot and functionalization of ZnMgO. *Adv. Opt. Mater.* **2024**, *12*, 2401085.

[38] Ma, S. L.; Cao, F.; Jia, G. H.; Wu, Q. Q.; Wang, S.; Yang, X. Y. Blue ZnSeTe quantum dot light-emitting diodes with low efficiency roll-off enabled by an *in situ* hybridization of ZnMgO nanoparticles and amino alcohol molecules. *Nanoscale* **2024**, *16*, 10441–10447.

[39] Han, C. Y.; Lee, S. H.; Song, S. W.; Yoon, S. Y.; Jo, J. H.; Jo, D. Y.; Kim, H. M.; Lee, B. J.; Kim, H. S.; Yang, H. More than 9% efficient ZnSeTe quantum dot-based blue electroluminescent devices. *ACS Energy Lett.* **2020**, *5*, 1568–1576.

[40] Jin, W. X.; He, S. Y.; Lu, X. Y.; Zhu, X. T.; Liu, D. J.; Sun, G. L.; Hao, Y. L.; Chen, Z. Y.; Wang, C. Y.; Zeng, J. J. et al. Water-induced high-performance quantum-dot light-emitting diodes. *Nat. Photon.* **2025**, *19*, 1233–1239.

[41] Zheng, Y. Z.; Lin, X.; Li, J. Z.; Chen, J. N.; Wu, W. H.; Song, Z. X.; Gao, Y.; Hu, Z.; Wang, H. F.; Ye, Z. K. et al. *In situ* N-doped nanocrystalline electron-injection-layer for general-lighting quantum-dot LEDs. *Nat. Commun.* **2025**, *16*, 3362.

[42] Chen, Z. N.; Chen, S. M. Eliminating positive aging in quantum dot light-emitting diodes by H_2O-treatment. *Adv. Mater.* **2025**, *37*, 2503477.

[43] Wang, S.; Liu, S. H.; Wang, T.; Bai, J. L.; Peng, J. Y.; Zhang, H. Z.; Xie, W. F.; Ji, W. Y. Operando ZnO recrystallization for efficient quantum-dot light-emitting diodes. *Light: Sci. Appl.* **2025**, *14*, 196.

[44] Wiles, C.; Watts, P. Recent advances in micro reaction technology. *Chem. Commun.* **2011**, *47*, 6512–6535.

[45] Watts, P.; Wiles, C. Recent advances in synthetic micro reaction technology. *Chem. Commun.* **2007**, 443–467

[46] Qi, D. W.; Xie, L. M.; Yang, M.; Meng, X. Q.; Yi, Y. Q. Q.; Hao, Y. F.; Su, W. M.; Xu, L.; Gai, Y. Q.; Cui, Z. Finely controlled synthesis of $Zn_{1-x}Mg_xO$ nanoparticles with uniform size distribution used as electron transport materials for red QLEDs. *ACS Appl. Electron. Mater.* **2022**, *4*, 1875–1881.

[47] Wang, T.; Xie, L. M.; Su, F. Y.; Meng, X. Q.; Song, Y. P.; Su, W. M.; Cui, Z. Sn-doped ZnO for efficient and stable quantum dot light-emitting diodes via a microchannel synthesis strategy. *Nanoscale* **2023**, *15*, 18523–18530.

[48] van Embden, J.; Gross, S.; Kittilstved, K. R.; Della Gaspera, E. Colloidal approaches to zinc oxide nanocrystals. *Chem. Rev.* **2023**, *123*, 271–326.

[49] Kim, H. H.; Kumi, D. O.; Kim, K.; Park, D.; Yi, Y.; Cho, S. H.; Park, C.; Ntwaeaborwa, O. M.; Choi, W. K. Optimization of the electron transport in quantum dot light-emitting diodes by codoping ZnO with gallium (Ga) and magnesium (Mg). *RSC Adv.* **2019**, *9*, 32066–32071.

[50] Liu, D. Q.; Cao, S.; Wang, S. Y.; Wang, H. Q.; Dai, W.; Zou, B. S.; Zhao, J. L.; Wang, Y. J. Highly stable red quantum dot light-emitting diodes with long T_{95} operation lifetimes. *J. Phys. Chem. Lett.* **2020**, *11*, 3111–3115.

[51] Shannon, R. D. Revised effective ionic radii and systematic studies of interatomic distances in halides and chalcogenides. *Acta Crystallogr. A: Found. Adv.* **1976**, *32*, 751–767.

[52] Mohanta, D.; Barman, K.; Jasimuddin, S.; Ahmaruzzaman, M. MnO doped SnO_2 nanocatalysts: Activation of wide band gap semiconducting nanomaterials towards visible light induced photoelectrocatalytic water oxidation. *J. Colloid Interface Sci.* **2017**, *505*, 756–762.

[53] Tan, S.; Park, S.; Choi, S. G.; Tye, O. J.; Zhang, R. Q.; Horowitz, J. R.; Terlier, T.; Chung, H.; Bulović, V.; Kwak, J. et al. Oxygen vacancy formation in ZnSeTe blue quantum dot light-emitting diodes. *J. Am. Chem. Soc.* **2025**, *147*, 40842–40848.

[54] Kim, H. M.; Kim, J.; Cho, S. Y.; Jang, J. Solution-processed metal-oxide p–n charge generation junction for high-performance inverted quantum-dot light-emitting diodes. *ACS Appl. Mater. Interfaces* **2017**, *9*, 38678–38686.

[55] Bruckdorfer, R. E.; Büttner, O. B.; Mau, G. "Flavor, fun, and vitamins"? Consumers' lay beliefs about child-oriented food products. *Appetite* **2025**, *205*, 107773

[56] Xie, L. M.; Li, Q.; Yi, Y. Q. Q.; Qiu, G. R.; Fayemi, O. E.; Mu, X. J.; Ma, Z. S.; Tang, P. Y.; Liu, Y.; Su, W. M. et al. High-performance inkjet-printed inverted QD-LEDs based on cross-linkable electron regulation layers. *Chem. Eng. J.* **2023**, *477*, 146789.